INTERNATIONAL JOURNAL FOR NUMERICAL METHODS IN FLUIDS, VOL. 25, 167–182 (1997)

AN IMPROVED NAVIER–STOKES PROCEDURE FOR ANALYSIS OF TWO-DIMENSIONAL AEROFOILS IN LAMINAR AND TURBULENT FLOWS

C. S. OH AND D. H. CHOI*

Department of Mechanical Engineering, Korea Advanced Institute of Science and Technology, Taejon, South Korea

SUMMARY

An accurate and robust Navier–Stokes procedure to predict the complex flow about an aerofoil has been developed. Much improvement over existing methods is achieved in various aspects of the solution procedure. The computational grid generated by conformal mapping, which is not only orthogonal but aligned with the inviscid streamlines, keeps the equations simple and minimizes the error due to false diffusion. Formal second-order accuracy is ensured by employing the QUICK scheme for the convective derivatives in the full Navier–Stokes and turbulence transport equations. To treat the separated region properly and to better resolve the flow field in the wake, the two-layer k–ε turbulence model is incorporated. The onset of transition is triggered in a unique fashion to warrant the smooth transition to turbulent flow. Sample calculations for various aerofoil sections show that the prediction is improved substantially over those by existing methods. The details of the flow extending to the wake, such as the surface pressure distribution, C_{Lmax}, the velocity fields and the Reynolds stress profiles, are found to be in excellent agreement with the data. © 1997 by John Wiley & Sons, Ltd.

Int. J. Numer. Meth. Fluids, **25**: 167–182 (1997)

No. of Figures: 15. No. of Tables: 0. No. of References: 20.

KEY WORDS: Navier–Stokes procedure; streamline co-ordinates; QUICK scheme; two-layer k–ε model; C_{Lmax}; near wake

1. INTRODUCTION

Aerodynamic characteristics of an aerofoil at incidence, especially near and beyond the stall angle, are of great practical interest as they dictate the performance of engineering devices such as aircraft and turbomachinery. Despite its seemingly simple geometry, the flow becomes quite complex: the region of separation increases with the angle of attack and the flow is dominated by the active viscous/inviscid interaction due to this large vortical motion. Further complication arises as it leaves the surface and develops into the wake, which in itself renders a great deal of scientific and engineering interest. The calculation of the entire flow, including the aerofoil and the wake, with reasonable accuracy and confidence becomes a formidable task.

Although some interactive methods[1–5] are sophisticated enough to give essential features of the flow, e.g., the C_{L}–α curve, they are incapable of handling the region beyond the separation point

* Correspondence to: D. H. Choi, Department of Mechanical Engineering, Korea Advanced Institute of Science and Technology, Taejon, South Korea

Contract grant sponsor: Korean Science and Engineering Foundation

CCC 0271–2091/97/020167–16 $17.50

Received October 1995
Revised September 1996

because of their boundary-layer type approach. To capture the flow structure of the vortical motion and the near wake, one must resort to the method based on the Navier–Stokes equations. The following are among many earlier attempts that fall in this category: Rhie and Chow[6] used a SIMPLE-type algorithm coupled with a k–ε turbulence model to predict the pressure distribution and the near wake; Shamroth[7] made compressible flow calculations using a transitional k–ε model; Rogers *et al.*[8] recently performed an incompressible flow calculation with the one-equation model of Baldwin and Barth. These calculations undoubtedly demonstrated some degree of success, but the results cannot be described as completely satisfactory: although the lift, which is an integrated quantity, seems reasonably well predicted, the local pressure and the velocity profiles were in noticeable disagreement with the data[9] against which the comparison was made. The indiscreet use of the k–ε model whether or not the actual flow is turbulent also needs careful scrutiny. Owing to the awkwardness in prescribing the turbulence quantities along the transition line, it is customary when using a k–ε model to assume the flow to be turbulent everywhere, since the laminar region is limited to the small region near the nose. All these features suggest that there is much to be improved in these methods.

The aim of this study is to develop an accurate and robust Navier–Stokes procedure to predict aerodynamic characteristics of an aerofoil and to resolve the details of the flow in the near wake. Although it is fully recognized that there is no shortage of studies concerning the flow structure of the near wake, it is also true that the leading-edge region or the entire aerofoil is seldom included in the calculations: an implication that it is difficult to obtain sufficiently good results in that part of the field which can be used with confidence for the downstream flow calculation. Among many factors that make accurate prediction difficult near the stall angle in particular are the presence of the large recirculating region and the increasing obliqueness of the flow direction with respect to the grid line. The latter is responsible for the growing numerical diffusion error. In an effort to minimize this false diffusion, we adopt the QUICK scheme together with streamline co-ordinates, in which the streamlines and the equipotential lines of the inviscid flow constitute the computational grids. Also, to better treat the flow in the separated region and thus in the wake, the two-layer k–ε turbulence model is incorporated in the study along with a novel treatment for transition to alleviate the aforementioned difficulty.

2. GRID GENERATION

For two-dimensional flows it is advantageous to use conformal mapping to generate orthogonal grids. The grids can also be made to be parallel to the inviscid flow streamlines with little additional effort. These two points are not imperative, but the equations become simpler when the co-ordinates are orthogonal and the numerical diffusion is greatly reduced if the streamline and the co-ordinate line coincide. It is therefore reasonable to expect the results to be more accurate.

An arbitrary aerofoil shape is mapped onto a unit circle by two successive transformations. The profile of length c with the trailing edge angle δ in the physical plane z is first transformed into a smooth, nearly circular section in the ζ-plane by the Karman–Trefftz transformation as was done by Theodorsen:[10]

$$\frac{z-\varepsilon}{z-c}=\left(\frac{\zeta+1}{\zeta-1}\right)^{p}, \qquad p=2\left(1-\frac{\delta}{2\pi}\right), \tag{1}$$

where the nodal point $(\varepsilon, 0)$ is taken at half the distance from the nose where the curvature becomes maximum to the center of curvature. This is then mapped into a unit circle in the τ-plane by solving the Gershgorin integral equation[11] numerically after the integrand has been suitably modified to make

the procedure more tractable and accurate. The details are given by Choi and Landweber[11] and will not be repeated here.

The resulting mapping function between the ζ- and τ-plane may be written as the Laurent series

$$\zeta = A\tau + a_1/\tau + a_2/\tau^2 + a_3/\tau^3 + \cdots, \tag{2}$$

where A and a are coefficients that are determined from the transformation. It is important to point out that since the profile in the intermediate plane ζ is nearly circular, the number of terms required in the series (2) to accurately compute ζ is not large: 10 terms have been found sufficient and used in the present work.

From these relations, various types of grid, i.e. C-, H- and O-type grids, can readily be constructed. The radial lines and concentric circles in the τ-plane give an O-type grid, while the horizontal and vertical lines in the plane of the complex potential W and those in the $W^{1/2}$-plane give H- and C-type grids respectively. The H-type grid is used in the present calculation and the details of how it is obtained are described below.

The complex potential W for a stream velocity U at an angle of attack α about a unit circle at the origin is

$$W = U\left(\tau e^{-i\alpha} + \frac{e^{i\alpha}}{\tau}\right) + i\frac{\Gamma}{2\pi}\ln\tau, \tag{3}$$

where Γ is the circulation about the circle and is equal to $4\pi U \sin(\alpha - \theta_0)$ so that equation (3) satisfies the Kutta condition, i.e. the velocity is zero at the trailing edge $\theta = \theta_0$. The velocity U in the τ-plane is related to the undisturbed velocity U_∞ in the z-plane by

$$U = U_\infty \left(\frac{d\zeta}{d\tau}\right)_\infty \left(\frac{dz}{d\zeta}\right)_\infty. \tag{4}$$

The co-ordinate lines in the W-plane are lines of constant potential ϕ and streamfunction ψ; the corresponding lines in the physical plane are also equipotential lines and streamlines of the flow under consideration and constitute an orthogonal H-type grid. It needs to be noted that when the circulation Γ is not zero, the potential at the trailing edge is double-valued, i.e.

$$\phi_{TU} = \phi_{TL} + \Gamma, \tag{5}$$

and a jump in ϕ is present across the trailing streamline.

For proper clustering in the streamwise direction, the grids are first distributed by using tanh along the stagnation streamline ABCD and AB′C′D shown in Figure 1. The transformed grids in the W-plane can then be obtained by using relations (1)–(3). However, a direct attempt to do so involves rather time-consuming algebra; the following spline interpolation is used instead. For a given set of points along the ϕ-axis, the corresponding points which lie on the stagnation streamline in the z-plane are readily determined: τ from (3) by Newton's root-finding algorithm, ζ by (2) and z by (1). The arc length s for each of these points is then calculated and the relation between s and ϕ is established. A cubic spline function is used to relate the two and for a point in the z-plane this interpolation function gives the corresponding point on the ϕ-axis in the W-plane. The grid clustering in the vertical direction, on the other hand, is done in the W-plane using ψ as a parameter. A typical grid for an NACA 4412 section at $\alpha = 13{\cdot}9^\circ$ is shown in Figure 2.

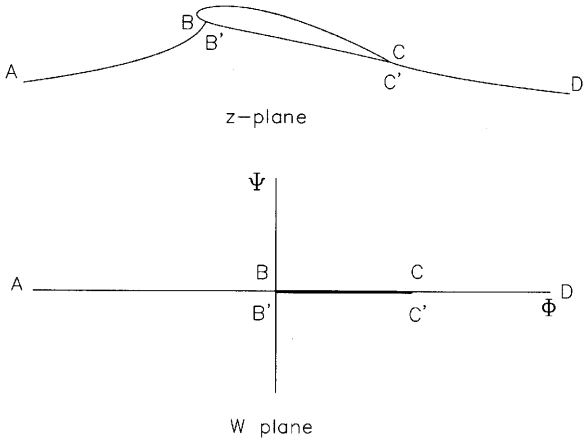

Figure 1. Physical and computational domains for flow about an aerofoil at incidence

3. GOVERNING EQUATIONS

Following Nash and Patel,[12] the continuity and Reynolds-averaged Navier–Stokes equations in general orthogonal curvilinear co-ordinates (ξ, η) for steady incompressible flows are written as follows:

continuity

$$\frac{1}{h_1 h_2}\left[\frac{\partial}{\partial \xi}(h_2 U) + \frac{\partial}{\partial \eta}(h_1 V)\right] = 0, \tag{6}$$

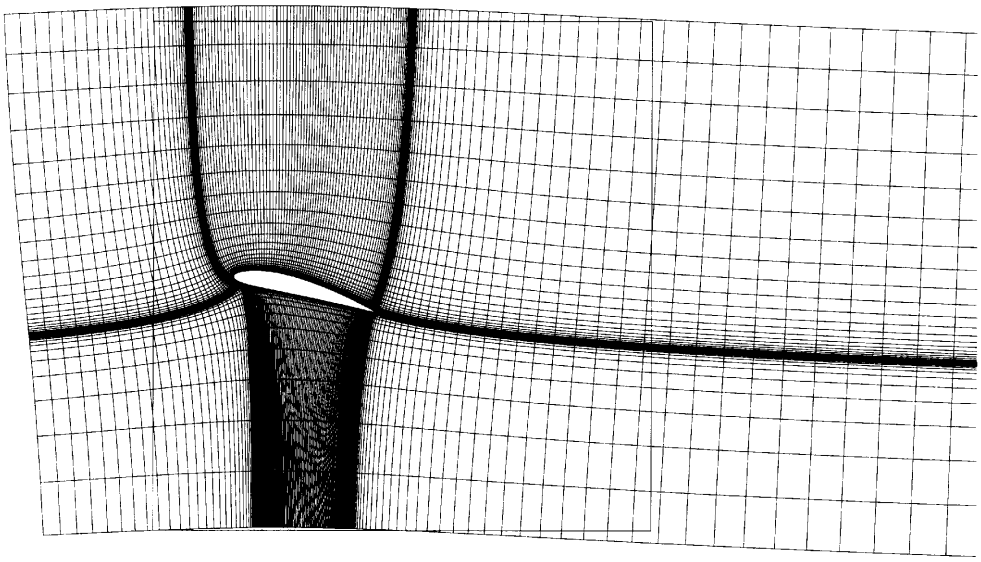

Figure 2. Sample grid for NACA 4412 aerofoil at $\alpha = 13{\cdot}9^\circ$

ξ-momentum

$$\frac{1}{h_1h_2}\frac{\partial}{\partial\xi}(h_2U^2)+\frac{1}{h_1h_2}\frac{\partial}{\partial\eta}(h_1UV)+(K_{12}U-K_{21}V)V$$
$$+\frac{1}{h_1}\frac{\partial p}{\partial\xi}+\frac{1}{h_1}\frac{\partial\overline{u^2}}{\partial\xi}+\frac{1}{h_2}\frac{\partial\overline{uv}}{\partial\eta}+2K_{12}\overline{uv}+K_{21}(\overline{u^2}-\overline{v^2})$$
$$-\frac{1}{Re}\left(\nabla^2U-2K_{21}\frac{1}{h_2}\frac{\partial V}{\partial\eta}+2K_{12}\frac{1}{h_1}\frac{\partial V}{\partial\xi}+\alpha_{11}U+\alpha_{12}V\right)=0, \tag{7}$$

η-momentum

$$\frac{1}{h_1h_2}\frac{\partial}{\partial\xi}(h_2UV)+\frac{1}{h_1h_2}\frac{\partial}{\partial\eta}(h_1V^2)+(K_{21}V-K_{12}U)U$$
$$+\frac{1}{h_2}\frac{\partial p}{\partial\eta}+\frac{1}{h_1}\frac{\partial\overline{uv}}{\partial\xi}+\frac{1}{h_2}\frac{\partial\overline{v^2}}{\partial\eta}+2K_{21}\overline{uv}-K_{12}(\overline{u^2}-\overline{v^2})$$
$$-\frac{1}{Re}\left(\nabla^2V-2K_{12}\frac{1}{h_1}\frac{\partial U}{\partial\xi}+2K_{21}\frac{1}{h_2}\frac{\partial U}{\partial\eta}+\alpha_{21}U+\alpha_{22}V\right)=0, \tag{8}$$

with

$$\nabla^2=\frac{1}{h_1h_2}\left[\frac{\partial}{\partial\xi}\left(\frac{h_2}{h_1}\frac{\partial}{\partial\xi}\right)+\frac{\partial}{\partial\eta}\left(\frac{h_1}{h_2}\frac{\partial}{\partial\eta}\right)\right],$$
$$\alpha_{11}=\alpha_{22}=-(K_{12}^2+K_{21}^2),$$
$$\alpha_{12}=\frac{1}{h_1}\frac{\partial K_{12}}{\partial\xi}-\frac{1}{h_2}\frac{\partial K_{21}}{\partial\eta},\qquad \alpha_{21}=\frac{1}{h_2}\frac{\partial K_{21}}{\partial\eta}-\frac{1}{h_1}\frac{\partial K_{12}}{\partial\xi},$$
$$K_{12}=\frac{1}{h_1h_2}\frac{\partial h_1}{\partial\eta},\quad \text{etc.},$$

where (U, V) and (u, v) are the mean and fluctuating velocity components respectively in the (ξ, η) direction, p is the pressure, Re is the Reynolds number, v is the kinematic viscosity and h and K are metric coefficients and curvature parameters respectively. The equations have been made dimensionless by using the freestream velocity U_∞ and the aerofoil chord c. These equations of conservative form appear to give more stable behaviour of the numerical method in the neighbourhood of the stagnation point where the H-grid becomes singular.

The Reynolds stresses in (7) and (8) are related to the mean rates of strain through the Boussinesq hypothesis:

$$-\overline{u^2}=-\tfrac{2}{3}k+2\nu_t\left(\frac{1}{h_1}\frac{\partial U}{\partial\xi}+K_{12}V\right), \tag{9}$$
$$-\overline{v^2}=-\tfrac{2}{3}k+2\nu_t\left(\frac{1}{h_2}\frac{\partial V}{\partial\eta}+K_{21}U\right), \tag{10}$$
$$-\overline{uv}=\nu_t\left(\frac{1}{h_1}\frac{\partial V}{\partial\xi}+\frac{1}{h_2}\frac{\partial U}{\partial\eta}-K_{12}U-K_{21}V\right), \tag{11}$$

where ν_t is the eddy viscosity to be determined from the turbulence model. Among many variations of the k–ε turbulence model, the two-layer model of Chen and Patel[13] is adopted in the present study.

This model modifies the standard k–ε model in the near-wall region: rather than resorting to the wall function approach to account for low-Reynolds-number effects, it uses the one-equation model of Wolfstein[14] and deduces the rate of dissipation ε from the algebraic relation with the kinetic energy k. The rest of the domain, i.e. the outer layer and the wake, is handled by the standard k–ε model. The boundary between one- and two-equation regions is placed at around $Re_y(=k^{1/2}y/\nu)=250$ as recommended by the originators. Figure 3 depicts these two regions in the transformed domain. The laminar portion of the flow, upstream of the transition location ξ_{tr} (region III in the figure), overlaps with the one- or two-equation region and the treatment of which will be explained later in this section.

The following two standard equations are solved for k and ε:

$$\frac{1}{h_1h_2}\frac{\partial}{\partial\xi}(h_2Uk)+\frac{1}{h_1h_2}\frac{\partial}{\partial\eta}(h_1Vk)-\frac{1}{h_1h_2}\left[\frac{\partial}{\partial\xi}\left(\frac{1}{\sigma_kR_{\text{eff}}}\frac{h_2}{h_1}\frac{\partial k}{\partial\xi}\right)+\frac{\partial}{\partial\eta}\left(\frac{1}{\sigma_kR_{\text{eff}}}\frac{h_1}{h_2}\frac{\partial k}{\partial\eta}\right)\right]-G+\varepsilon=0, \tag{12}$$

$$\frac{1}{h_1h_2}\frac{\partial}{\partial\xi}(h_2U\varepsilon)+\frac{1}{h_1h_2}\frac{\partial}{\partial\eta}(h_1V\varepsilon)-\frac{1}{h_1h_2}\left[\frac{\partial}{\partial\xi}\left(\frac{1}{\sigma_\varepsilon R_{\text{eff}}}\frac{h_2}{h_1}\frac{\partial\varepsilon}{\partial\xi}\right)+\frac{\partial}{\partial\eta}\left(\frac{1}{\sigma_\varepsilon R_{\text{eff}}}\frac{h_1}{h_2}\frac{\partial\varepsilon}{\partial\eta}\right)\right]-C_{\varepsilon1}\frac{\varepsilon}{k}G+C_{\varepsilon2}\frac{\varepsilon^2}{k}=0, \tag{13}$$

where

$$\nu_t=C_\mu k^2/\varepsilon, \tag{14}$$

$$G=-\overline{uv}\left(\frac{1}{h_1}\frac{\partial V}{\partial\xi}+\frac{1}{h_2}\frac{\partial U}{\partial\eta}-K_{12}U-K_{21}V\right)-(\overline{u^2}-\overline{v^2})\left(\frac{1}{h_1}\frac{\partial U}{\partial\xi}+K_{12}V\right), \tag{15}$$

$$1/R_{\text{eff}}=1/Re+\nu_t \tag{16}$$

and the constants are $C_\mu=0{\cdot}09$, $C_{\varepsilon1}=1{\cdot}44$, $C_{\varepsilon2}=1{\cdot}92$, $\sigma_k=1{\cdot}0$ and $\sigma_\varepsilon=1{\cdot}3$. The rate of dissipation and the eddy viscosity in the wall region are determined by

$$\varepsilon=k^{3/2}/l_\varepsilon, \tag{17}$$

$$\nu_t=C_\mu k^{1/2}l_\mu, \tag{18}$$

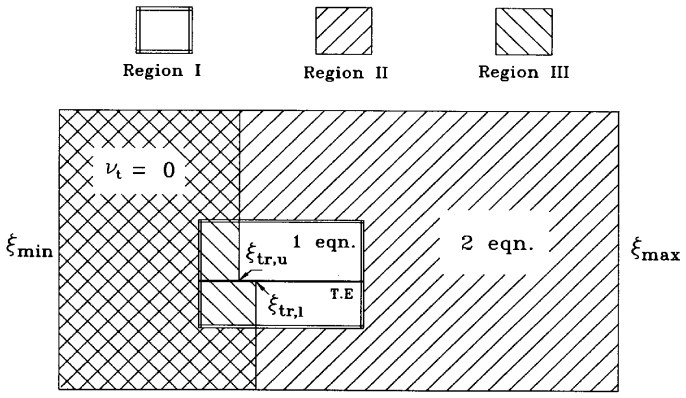

Figure 3. Treatment of various regions with two-layer k–ε model

with

$$l_\mu = C_l\, y[1 - \exp(-Re_y/A_\mu)], \qquad l_\varepsilon = C_l y[1 - \exp(-Re_y/A_\varepsilon)],$$

where $C_l = \kappa C_\mu^{-3/4}$, $A_\mu = 70$, $A_\varepsilon = 2C_l$ and $\kappa = 0{\cdot}418$ is the von Karman constant. The derivation of these model constants is given in Reference 13 and will not be repeated here. This eliminates the need for a low-Reynolds-number-effect correction in the ε-equation and yet the model is superior to the wall function approach, since not only is it capable of handling the reversed flow region but also it naturally provides finer grid resolution in the wake.

Obviously, the transport equations for k and ε need to be invoked only in the turbulent flow region. However, the initial conditions for k and ε at the transition point, which are accurate and compatible with the other flow variables, are cumbersome if not impossible to prescribe and the errors introduced inevitably may take a few steps to decay. Ignoring the leading edge laminar region altogether is difficult to justify, however small the region may be, as the artificially produced turbulent boundary layer, which is healthier than the real flow, could greatly affect the leading edge separation pattern. As we shall see later, the downstream flow is very sensitive to the transition location. To ensure smooth transition, the equations are solved for the entire domain but the eddy viscosity is artificially set to be zero in the laminar region (see Figure 3). The procedure has been found successful in simulating the transition behaviour.

4. SOLUTION PROCEDURE

The equations described in the previous section, i.e. equations (6)–(8), (12) and (13), are solved using the SIMPLER algorithm[15] on a staggered grid. While the equations are discretized mainly by central differencing, the higher-order upwind (QUICK) scheme of Hayase *et al.*[16] is adopted for the convective derivatives to maintain the second-order accuracy and also to avoid the unrealistic oscillatory behaviour of the solution. Depending on the sign of the streamwise velocity, the dependent variable ϕ at the interface $i + \frac{1}{2}$ is expressed as

$$\phi_{i+1/2} = \phi_i + \tfrac{1}{8}(-\phi_{i-1} - 2\phi_i + 3\phi_{i+1}) \quad \text{if } u_{i+1/2} \geq 0, \tag{19}$$

$$\phi_{i+1/2} = \phi_{i+1} + \tfrac{1}{8}(3\phi_i - 2\phi_{i+1} - \phi_{i+2}) \quad \text{if } u_{i+1/2} < 0. \tag{20}$$

These relations were devised from the original QUICK formulation of Leonard[17] by requiring the coefficients to satisfy four rules[15] that ensure physically realistic solutions. This version of the QUICK scheme was reported[16] and confirmed during the course of this study to be more stable and converge faster than others.

The computational domain, bounded by the lines of constant ξ and η, is chosen sufficiently large; the following boundary conditions may then be applied:

$$\text{upstream} \quad U = U_{\text{pot}}, \quad \frac{\partial V}{\partial \xi} = 0, \quad k = \varepsilon = 10^{-10},$$

$$\text{downstream} \quad \frac{\partial p}{\partial \xi} = 0, \quad \frac{\partial^2}{\partial \xi^2} = 0 \quad \text{for } U, V, k, \varepsilon,$$

$$\text{outer} \quad \frac{\partial U}{\partial \eta} = 0, \quad V = V_{\text{w}}, \quad \frac{\partial k}{\partial \eta} = \frac{\partial \varepsilon}{\partial \eta} = 0,$$

$$\text{surface} \quad \text{no-slip condition},$$

where the subscript 'pot' denotes the potential flow value. The underlying bases for these conditions are mostly obvious. The small upstream values of k and ε mean that the flow is free of turbulence

there. The cross-stream velocity component V_w is prescribed along the outer boundary to simulate the effects of the wind-tunnel wall when it is present. The value for V_w is updated after each iteration to make the flow parallel to the wall. The solution is sought iteratively: one global iteration cycle comprises the usual velocity–pressure coupling steps of SIMPLER, i.e. calculations of pseudovelocity, pressure, velocity and velocity correction in succession, followed by the solution of the turbulence transport equations. An ADI scheme is used to solve each equation; the solution is considered to have converged when the following criterion is met:

$$\sum(|\mathrm{Res}_Q|) < 10^{-5} \quad (Q, \text{ continuity equation}).$$

A typical turbulent flow calculation with a 180×60 grid for Re in millions requires a few hundred iterations and takes about 15–20 min of CPU time on an HP735 (99 MHz) workstation.

5. RESULTS AND DISCUSSION

To validate the procedure described in the previous section, it is first applied to calculate the laminar flow about a 12 per cent-thick Joukowski aerofoil and the surface pressure distribution for $\alpha = 5^\circ$ and $Re = 1000$ is presented in Figure 4. It is easy to see that the present solution is grid-independent, as two different grids, i.e. 65×30 and 120×60, give identical results. The excellent agreement with the results of Ghia *et al.*[18] confirms that the present method is accurate and efficient.

For turbulent flows, three different aerofoil sections, namely an NACA 4412 and two models of Nakayama,[19] have been chosen for comparison, mainly because they provide extensive data both on the aerofoil and in the wake.

The flow about an NACA aerofoil section at $\alpha = 13{\cdot}9^\circ$ is close to where the aerofoil attains the maximum lift for $Re = 1{\cdot}5 \times 10^6$ and has been one of the popular test cases owing to its complexity. The calculation is performed on a 180×60 grid, which is fitted over $-1{\cdot}5 \leqslant x/c \leqslant 10$, with the first grid off the surface, near $x/c \approx 0{\cdot}5$, being placed at $y^+ \approx 1$ (see Figure 2). The grid density and domain size have been checked thoroughly to insure that the solution is independent of these factors. It is appropriate to note here that the grid needs to be reconstructed when the angle of attack or the Reynolds number changes. The vertical boundary is located where the tunnel wall is to closely mimic the experimental condition. Since the ceiling or the floor does not coincide with the constant η line as indicated in Figure 2, a small amount of vertical velocity component is introduced to make the velocity vector parallel to the wall as was mentioned in the previous section. The transition for the upper and lower surfaces is triggered at $x/c = 0{\cdot}025$ and $0{\cdot}103$ respectively as done in the

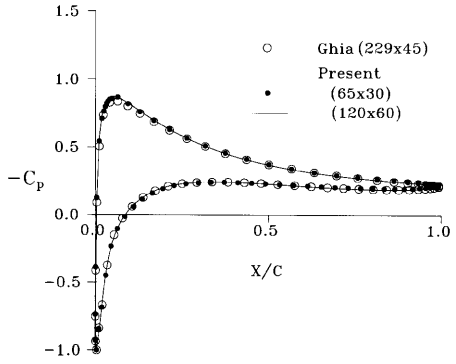

Figure 4. Surface pressure distribution for 12 per cent-thick Joukowski aerofoil at $\alpha = 5^\circ$ and $Re = 1000$

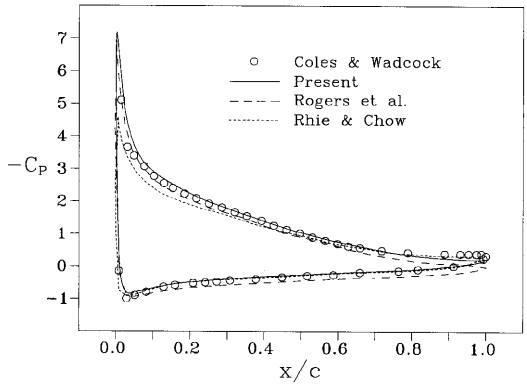

Figure 5. Surface pressure distribution for NACA 4412 aerofoil at $\alpha = 13{\cdot}9^\circ$ and $Re = 1{\cdot}5 \times 10^6$

experiment.[9] This is achieved by letting v_t assume the calculated value downstream of these points while keeping v_t zero in the upstream region as explained earlier. The surface pressure distribution, which is presented in Figure 5, is seen to be in close agreement with the measured data. The improvement over the results of Rhie and Chow[6] and Rogers *et al.*[8] is clear, as those deviate considerably from the measured data especially in the leading or trailing edge region.

The skin friction distribution for the upper surface depicted in Figure 6 indicates that the flow separates at $x/c = 0{\cdot}8$ as was experimentally observed.[9] The sharp increase in C_f is typical of the transition behaviour as the boundary layer profile changes from laminar to turbulent and is seen to be nicely simulated in the calculation. This serves as clear evidence that the present treatment of bridging the laminar and turbulent regions is qualitatively correct. One could also see that, had the transition not been triggered, the laminar boundary layer would have separated very early. The mean velocity profiles and Reynolds shear stress profiles at various stations are plotted in Figures 7 and 8 respectively. The good correlation with the measured mean velocity data observed in the boundary layer is particularly rewarding, as most other methods had difficulty in predicting it as compared in the figure. The degrading agreement in the wake region may partially be attributed to the difference in co-ordinate systems: some undue error could have crept in during transformation and interpolation of the velocity components. By the same token, the measured Reynolds stress in Figure 8 is presented only as a reference, because the measured and computed stresses are not in the same co-ordinates and the difference cannot possibly be resolved.

Figure 9 compares the pressure distributions for the same aerofoil at $\alpha = 10^\circ$ in order to highlight the superiority of the streamline co-ordinates. The calculations are made with two different grids: one generated for the flow of interest, i.e. $\alpha = 10^\circ$, and the other for $\alpha = 2^\circ$. Both grids are orthogonal and

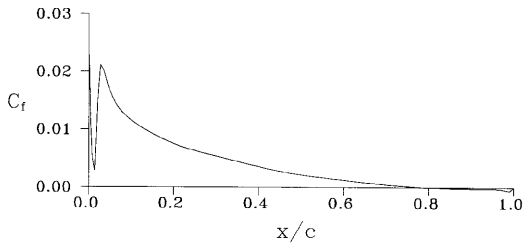

Figure 6. Skin friction distribution on upper surface of NACA 4412 aerofoil at $\alpha = 13{\cdot}9^\circ$ and $Re = 1{\cdot}5 \times 10^6$

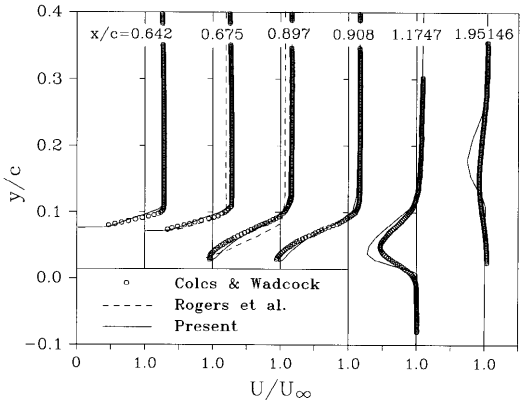

Figure 7. Streamwise mean velocity profiles for NACA 4412 aerofoil at $\alpha = 13{\cdot}9^\circ$ and $Re = 1{\cdot}5 \times 10^6$

of density 140×40. However, the agreement between the two is very poor on the upper surface in general. Interestingly, the discrepancy vanishes as the grid density for $\alpha = 2^\circ$ is increased to 186×60. Key conclusions can be drawn from this figure, namely that the solution by the 10°, 140×40 grid is correct and, because of the numerical diffusion, the non-streamline co-ordinates need a denser grid distribution to obtain comparable results. It is also experienced that making the solution converge is more difficult with the non-streamline grids.

A series of calculations for various angles of attack produces the C_L–α curve in Figure 10; the agreement with the data is again excellent. Key characteristics of the aerofoil, such as the maximum lift coefficient $C_{L\max}$ and the subsequent stall, are very well predicted. This demonstrates that the method is capable of handling flow with large separation and can be applied to calculate the post-stall flow.

To further evaluate the performance of the procedure, particularly in the wake region, calculations have also been carried out for the aerofoil sections tested by Nakayama, for which an extensive set of boundary layer and wake data is available. One of the models, designated as model A in Reference 19, is a 10 per cent-thick conventional aerofoil and the other (model B) is a 14 per cent-thick supercritical aerofoil, whose lower surface near the trailing edge is severely curved (see Figure

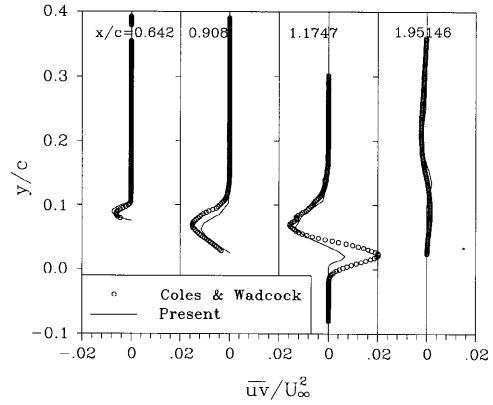

Figure 8. Reynolds shear stress ($\overline{uv}$) profiles for NACA 4412 aerofoil at $\alpha = 13{\cdot}9^\circ$ and $Re = 1{\cdot}5 \times 10^6$

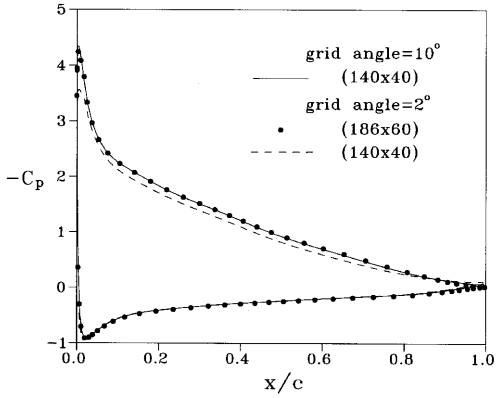

Figure 9. Surface pressure distribution for NACA 4412 aerofoil at $\alpha = 10^\circ$ and $Re = 1{\cdot}5 \times 10^6$ by two different grids illustrating advantages of streamline co-ordinates

11(b)). The Reynolds numbers for both test cases are kept constant at $1{\cdot}2 \times 10^6$ and the angles of attack are 0° and 4° for models A and B, respectively.

The calculation domain is chosen in the same way as above and the boundary layer trips for the upper and lower surfaces are made at $x/c = 0{\cdot}16$ and $0{\cdot}05$ respectively as in the experiment. Figure 11 shows the pressure distributions for both cases, which are in perfect agreement with the data. Predicting the pressure in these cases may not be very demanding, as the boundary layer is mostly attached. More significant are the next two figures that compare the mean velocity and Reynolds stress profiles. The mean velocity profiles both in the boundary layer and in the wake correlate extremely well with the measured data as seen in Figure 12. Here y_c denotes the wake centreline along which the velocity becomes minimum as illustrated in the figure. It should be noted that the calculation for model B was repeated with the transition on the lower surface prescribed at $x/c = 0{\cdot}4$, further downstream of the trip location, on the basis of the experimental observation that the real boundary layer was too stable to become turbulent until a long way past the trip wire.[20] The broken

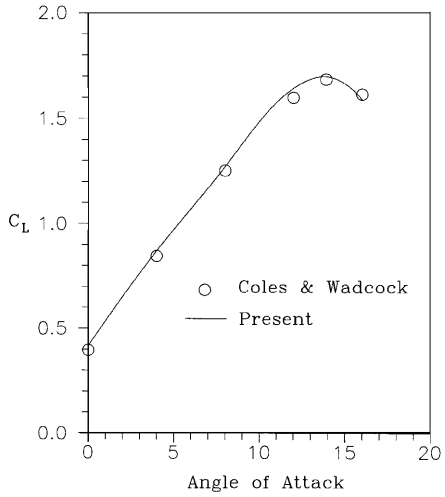

Figure 10. C_L–α curve for NACA 4412 aerofoil section at $Re = 1{\cdot}5 \times 10^6$

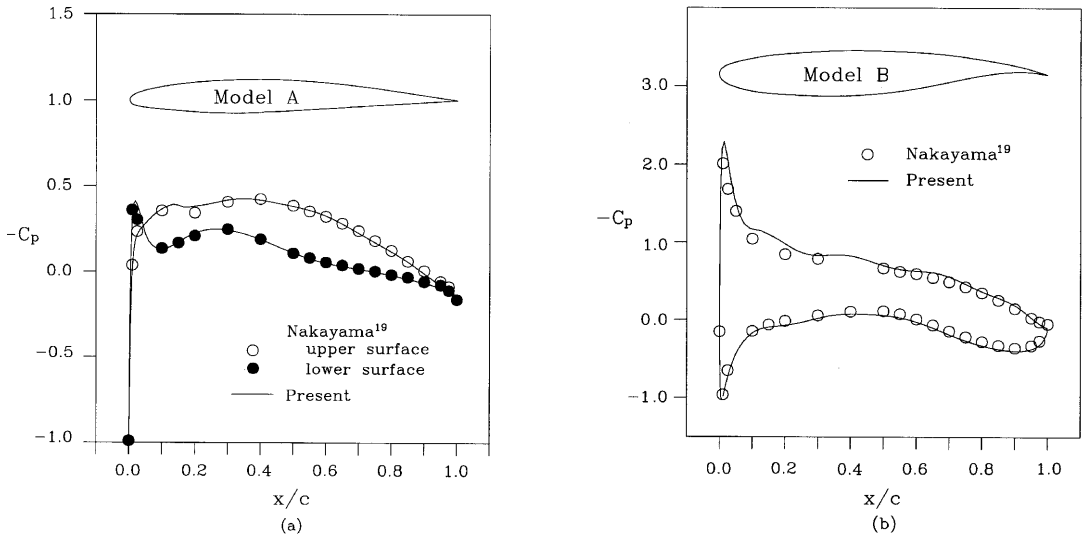

Figure 11. Surface pressure distribution for $Re = 1{\cdot}2 \times 10^6$: (a) model A, $\alpha = 0°$; (b) model B, $\alpha = 4°$

lines in Figures 12(b) and 13(b), which represent the results with the transition at $x/c = 0{\cdot}05$, overpredict the boundary layer and the wake as a consequence of the fact that the boundary layer has been in the turbulent state for a longer distance. The results point out that the downstream development of the boundary layer may depend heavily on the transition location and therefore its prescription should not be taken lightly to ensure an accurate flow prediction. The Reynolds shear stress profiles at various locations are then plotted in Figure 13 to examine how well the turbulence structure is captured. Here the boundary layer portion of model B is omitted since the co-ordinates for the computation and the measurement do not match in this region. The agreement with the data for model A is again found to be superb. On the other hand, for model B, although the profiles for the upper half of the wake look still very respectable, the results for the lower half do not compare as favourably. The turbulence production in the region could have been enhanced by the highly curved local streamlines in connection with the severely concave lower surface (see Figure 11(b)). The sizable discrepancy observed in the figure obviously suggests that some work needs to be done to improve the results in the region. Although no attempts have been made in this regard, the turbulence model that takes into account the streamline curvature effects should perform more successfully for this type of flow.

Finally, two key integral parameters, namely the skin friction and the displacement thickness, are presented in Figures 14 and 15 to see the global view of the code performance. The calculated values of δ^* in the wake denoted by symbols look somewhat rough because of the interpolation involved. The good correlation of these quantities for the boundary layer and the wake assures that almost every detail of the flow structure is satisfactorily predicted by the present method.

6. CONCLUSIONS

An improved Navier–Stokes procedure has been developed and applied successfully to various aerofoil sections. It is demonstrated through a series of calculations that the flow details of aerodynamic interest both on the surface and in the wake can be accurately predicted. The method is

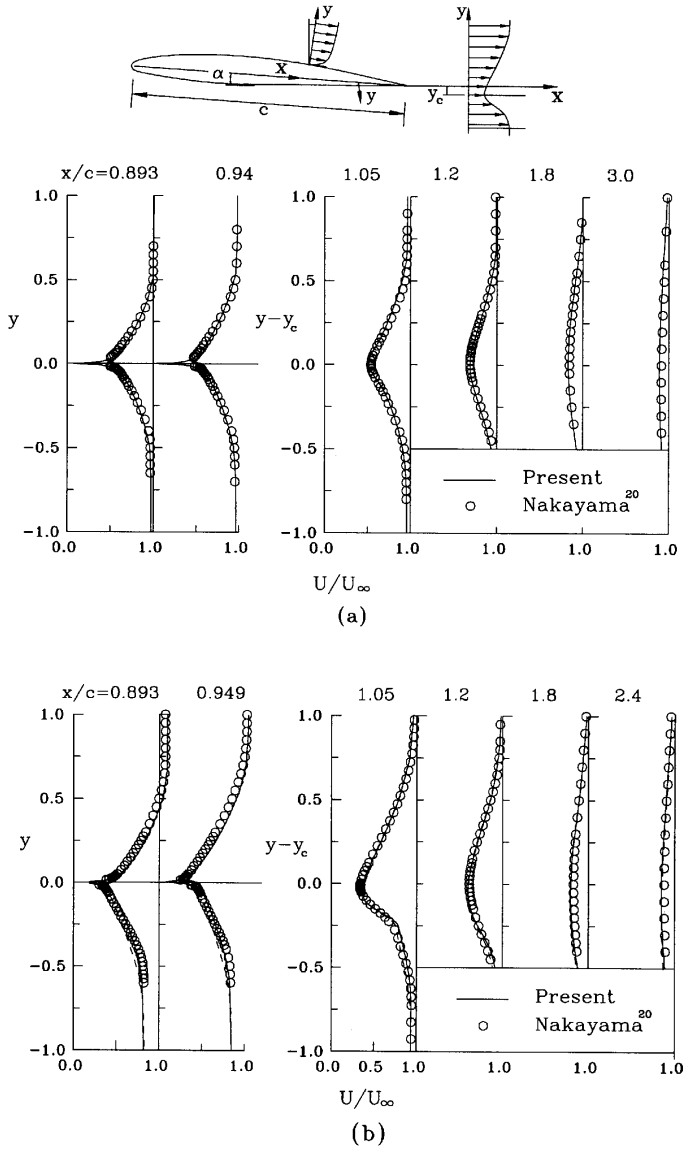

Figure 12. Mean velocity profiles at various streamwise stations for $Re = 1{\cdot}2 \times 10^6$: (a) model A, $\alpha = 0°$; (b) model B, $\alpha = 4°$

second-order accurate; the present choice of the co-ordinates, i.e. the streamlines and the equipotential lines of the inviscid flow, together with the turbulence model which is applicable to the reversed flow region, and the novel treatment of the transition, all help place the method above the existing ones.

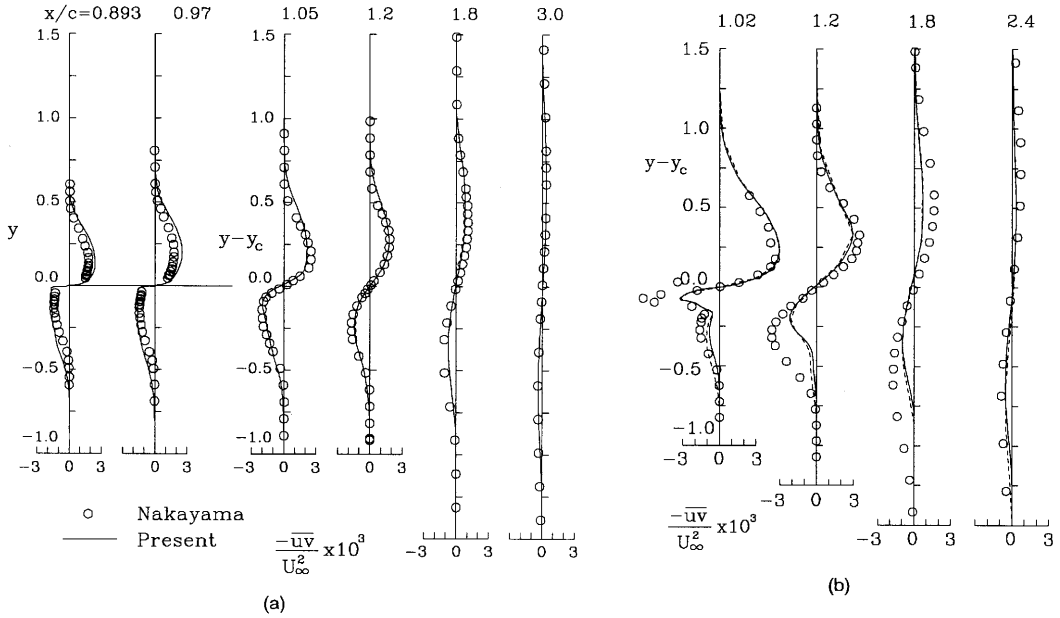

Figure 13. Reynolds shear stress ($\overline{uv}$) profiles at various streamwise stations for $Re = 1{\cdot}2 \times 10^6$: (a) model A, $\alpha = 0°$; (b) model B, $\alpha = 4°$

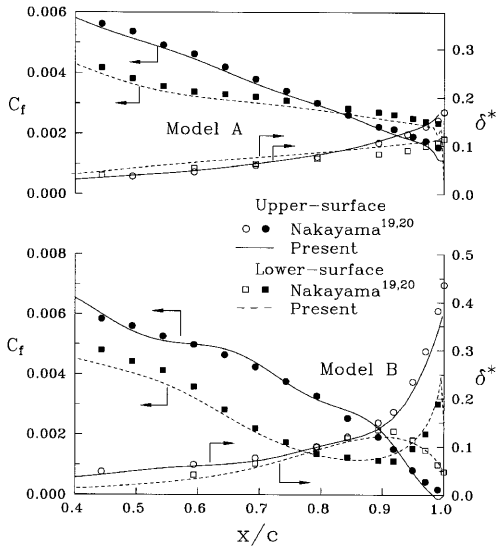

Figure 14. Skin friction coefficient and displacement thickness distribution in boundary layer: full symbols, C_f; open symbols, δ^*

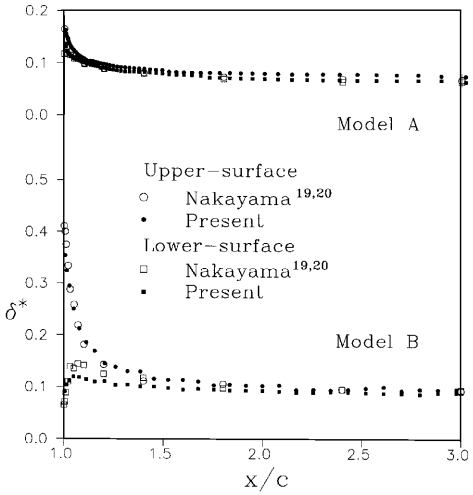

Figure 15. Displacement thickness distribution in wake

ACKNOWLEDGEMENT

This work was supported by the Korea Science and Engineering Foundation under Grant 931-1000-024-2.

REFERENCES

1. B. Maskew and F. A. Dvorak, 'The prediction of C_{Lmax} using a separated flow model', *J. Am. Helicopter Soc.*, (1978).
2. B. R. Gilmer and D. R. Bristow, 'Analysis of aerofoils by simultaneous perturbations to viscous and inviscid equations', *AIAA J.*, **20**, 1160–1166 (1982).
3. R. C. Lock and M. C. P. Firmin, 'Survey of techniques for estimating viscous effects in external aerodynamics', in P. L. Roe (ed.), *Numerical Methods in Aeronautical Fluid Dynamics*, Academic, New York, 1982, pp. 337–430.
4. M. Ribaut, 'A vortex sheet method for calculating separated two-dimensional flows', *AIAA J.*, **21**, 1079–1086 (1983).
5. T. Cebeci, J. Jau, D. Vitiello and K. C. Chang, 'Prediction of post-stall flows on aerofoils', *Proc. 4th Symp. on Numerical and Physical Aspects of Aerodynamic Flows*, Long Beach, CA, January 1989.
6. C. M. Rhie and W. L. Chow, 'Numerical study of the turbulent flow past an aerofoil with trailing edge separation', *AIAA J.*, **21**, 1525–1532 (1983).
7. S. J. Shamroth, 'Calculation of steady and unsteady aerofoil flow fields via the Navier–Stokes equation', *NASA CR-3899*, 1985.
8. S. E. Rogers, N. L. Wiltberger and D. Kwak, 'Efficient simulation of incompressible viscous flow over multi-element aerofoils', *Proc. 5th Symp. on Numerical and Physical Aspects of Aerodynamic Flows*, Long Beach, CA, January 1992.
9. D. Coles and A. J. Wadcock, 'Flying-hot-wire study of two-dimensional mean flow past a NACA4412 aerofoil at maximum lift', *AIAA J.*, **17**, 321–329 (1979).
10. T. Theodorsen, 'Theory of wing sections of arbitrary shapes', *NACA TR 411*, 1931.
11. D. H. Choi and L. Landweber, 'Inviscid analysis of two-dimensional aerofoils in unsteady motion using conformal mapping', *AIAA J.*, **28**, 2025–2033 (1990).
12. J. F. Nash and V. C. Patel, *Three Dimensional Turbulent Boundary Layers*, BC Technical Books, Atlanta, GA, 1972.
13. H. C. Chen and V. C. Patel, 'Near-wall turbulence models for complex flows including separation', *AIAA J.*, **26**, 641–648 (1988).
14. M. Wolfstein., 'The velocity and temperature distribution in one dimensional flow with turbulence augmentation and pressure gradient', *Int. J. Heat Mass Transfer*, **12**, 301–318 (1969).
15. S. V. Patankar, *Numerical Heat Transfer and Fluid Flow*, McGraw– Hill, New York, 1980.
16. T. Hayase, J. A. C. Humphrey and R. Grief, 'A consistently formulated QUICK scheme for fast and stable convergence using finite-volume iterative calculation procedures', *J. Comput. Phys.*, **98**, 108–118 (1992).
17. B. P. Leonard, 'A stable and accurate convective modelling procedure based on quadratic upstream interpolation', *Comput. Methods Appl. Mech. Eng.*, **19**, 59–98 (1979).

18. K. N. Ghia, G. A. Osswald and U. Ghia, 'Analysis of two-dimensional incompressible flow past aerofoils using unsteady Navier–Stokes equations', in T. Cebeci (ed.), *Proc. Symp. on the Numerical and Physical Aspects of Aerodynamic Flows III*, Springer, New York, 1985, pp. 318–338.
19. A. Nakayama, 'Characteristics of the flow around conventional and supercritical aerofoils', *J. Fluid Mech.*, **160**, 155–179 (1985).
20. A. Nakayama, Personal communication, 1995.

